

# Winding-Control Mechanism of Non-Hermitian Systems

Yongxu Fu<sup>1,\*</sup> and Yi Zhang<sup>2,†</sup>

<sup>1</sup>*Department of Physics, Zhejiang Normal University, Jinhua 321004, China*

<sup>2</sup>*International Center for Quantum Materials, School of Physics, Peking University, Beijing 100871, China*

Non-Hermitian quantum systems exhibit various interesting and inter-connected spectral, topological, and boundary-sensitive features. By introducing conditional boundary conditions (CBCs) for non-Hermitian quantum systems, we explore a winding-control mechanism that selectively collapses specific periodic boundary condition (PBC) spectra onto their open boundary condition (OBC) counterparts, guided by their specific winding numbers, together with a composite reconstruction of the Brillouin zone (BZ) and generalized Brillouin zone (GBZ). The corresponding eigenstates also manifest nontrivial skin effects or extended behaviors arising from the interplay between BZ and GBZ structures. Furthermore, we can generalize our control by incorporating similarity transformations and holomorphic mappings with the boundary controls. We demonstrate the winding control numerically within various models, which enriches our knowledge of non-Hermitian physics across the spectrum, topology, and bulk-boundary correspondence.

*Introduction.*— The burgeoning field of non-Hermitian physics has attracted significant attention [1–25], due to its capacity to effectively capture open quantum systems [26–30], optical systems [31–36], electric circuit simulations [37–41], classical mechanical platforms [42–47], among others. A key hallmark is their striking sensitivity to boundary conditions, such as the non-Hermitian skin effect (NHSE) where an extensive number of eigenstates accumulate at boundaries under open boundary conditions (OBCs), in stark contrast to their counterparts under periodic boundary conditions (PBCs) [10, 12]. This theoretical cornerstone in non-interacting cases has prompted advances across various areas of condensed matter physics, including localization versus delocalization [48–53], quantum entanglement [54–61], as well as the NHSE in dynamical and many-body systems [62–70].

The anomalous boundary sensitivity has challenged conventional bulk-boundary correspondences and motivated the generalized Brillouin zone (GBZ) formalism, which precisely characterizes the bulk spectrum under OBCs by generalizing the Bloch momenta within the Brillouin zone (BZ) to the complex plane [10, 12]. Fine-tuned couplings between the two ends of one-dimensional (1D) chains uncover various exotic behaviors, including the emergent scale-free localization [41, 71–75]. However, the underlying mechanism and targeted control of such boundary sensitivity and fine-tuning, especially in general scenarios such as multiple PBC spectral loops, remain obscure.

In this paper, we propose a winding-based control theory and formalism, revealing and relying on the intimate connections between spectrum, GBZ, winding number, and boundary conditions in general. By introducing conditional boundary conditions (CBCs) with exclusive hopping, we can selectively collapse pieces of the PBC spectrum to their OBC counterparts according to their re-

spective winding numbers, accompanied by a composite reconstruction of corresponding segments of the BZ and GBZ between the Bloch points separating different winding domains. Such a hybrid spectral structure gives rise to eigenstates with nontrivial localization properties, which cannot be understood from the perspective of either the BZ or GBZ alone. Furthermore, through holomorphic mappings, including simple similarity transformations, we achieve further control over the relative figures of the BZ and GBZ before CBC implementations, paving the way for systematic control over non-Hermitian spectra and band structures. We demonstrate the accuracy and versatility of our control with multiple 1D non-Hermitian lattice models.

*Winding-control mechanism via imaginary velocity and boundary conditions.*— Given a 1D non-interacting fermionic non-Hermitian Hamiltonian  $\hat{H}$  [76], we are interested in the Fermi Sea with all single-particle states with  $\text{Re}(\epsilon) < 0$  filled and with  $\text{Re}(\epsilon) > 0$  empty [77]. For a band with two Fermi points  $\text{Re}(\epsilon_{F,2}) = \text{Re}(\epsilon_{F,1}) = 0$  [78], the velocity expectation value equals:

$$\bar{v} = \sum_{\text{Re}(\epsilon_z) < \mu} v_z = (\epsilon_{F,2} - \epsilon_{F,1})L/2\pi, \quad (1)$$

where the summation is over the BZ or GBZ between the Fermi points. While  $\bar{v}$  vanishes for a Hermitian  $\hat{H}$ , it may obtain a residue imaginary part in non-Hermitian quantum systems, as  $\text{Im}(\epsilon_{F,1})$  and  $\text{Im}(\epsilon_{F,2})$  may differ [Fig. 1(b)]. Such an  $\text{Im}(\bar{v})$  is related to the Fermi Sea’s collective quasiparticle displacements in imaginary time  $\tau = it \in \mathbb{R}$  and may carry profound physical consequences, such as a mechanism and diagnosis for delocalization [53] and the circulation of path-integral worldlines [Fig. 1(a)] in space-time  $(x-\tau)$  [53, 79]. Correspondingly, the worldline winding number  $W$  is related to  $\text{Im}(\bar{v})$ :

$$W = \text{Im}(\bar{v})\beta/L, \quad (2)$$

where  $\beta = 1/k_B T$  is the inverse temperature and  $L$  is the system size. Following straightforwardly from Eq. (1),  $W$  may become nonzero under PBCs but is guaranteed

\* yongxufu@zjnu.edu.cn

† frankzhangyi@pku.edu.cn

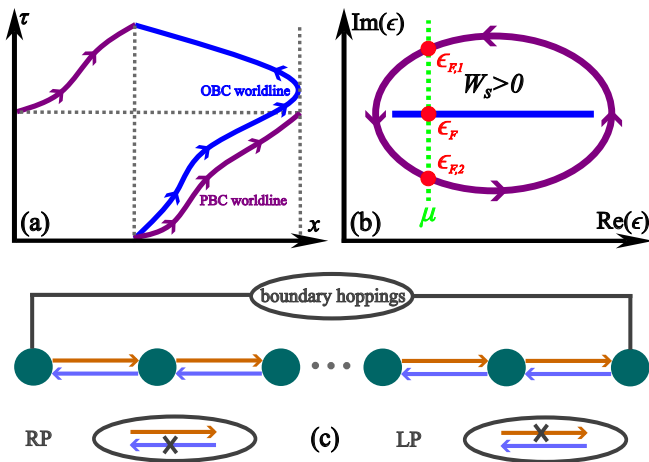


FIG. 1. (a) Schematically, a worldline may wind around the system under PBCs (purple), yet its winding number must be trivial under OBCs (blue). (b) The Fermi points  $\epsilon_{F,1}$ ,  $\epsilon_{F,2}$ , and  $\epsilon_F$  are intersections of the spectra (purple under PBCs and blue under OBCs) with the Fermi energy  $\mu$  (green dashed line), resulting in an imaginary velocity  $\text{Im}(\bar{v}) < 0$  and spectral winding  $W_s > 0$  under PBCs, and vanishing  $\text{Im}(\bar{v})$  and  $W_s$  under OBCs, following the spectrum-velocity-winding relations in Eqs. (1)-(3). (c) The RP (LP) CBC fully suppresses the left-bound (right-bound) hoppings across the boundary, admitting only non-negative (non-positive)  $\bar{v}$  and non-positive (non-negative)  $W_s$ .

to vanish under OBCs [Fig. 1(a)]. These relations have been precisely confirmed in QMC-SSE calculations [53, 79].

Crucially, the worldline winding number  $W$  is closely connected to the spectral winding number  $W_s$  of the PBC spectrum, as exemplified by a single-band model with energy dispersion  $\epsilon_z$ :

$$W_s = \frac{1}{2\pi} \oint_{z \in \text{BZ}} d \arg(\epsilon_z - \epsilon_0), \quad (3)$$

where  $\epsilon_0$  is an arbitrary reference energy inside the spectral loop and the BZ is the unit circle in the complex plane. Given a specific Fermi energy  $\mu$ , a positive  $\text{Im}(\bar{v})$  corresponds to a positive  $W$ , right-bound quasiparticles and worldlines, and a negative  $W_s$ , and vice versa [79]. Notably, the counterclockwise contour integration [Fig. 1(b)] introduces a sign inversion for  $W_s$  in our convention. We note that boundary conditions can significantly influence such directional flows. The simplest and most straightforward case is the OBC, which forces  $\bar{v}$  to vanish and constrains the spectrum: except for spectral endpoints, all energy contours must be doubly degenerate under OBCs, irrespective of whether  $\hat{H}$  is Hermitian or non-Hermitian, single-band or multi-band; otherwise, there always exists a traversing Fermi energy  $\mu$  leading to a contradictory nonzero  $\bar{v}$ ; see details in Supplementary Materials [80]. Simultaneously, the halted quasiparticle flow leads to state accumulations at open boundaries—a defining signature of the NHSE and generalizable to

higher-dimensional or many-body NHSE [70, 81].

Similarly, if we can selectively manipulate the winding numbers through boundary conditions or alternative schemes, we can piecewise modify the corresponding spectra and GBZ, which underpins our winding-based control mechanism. For instance, consider a segment of a PBC spectrum and BZ with  $W_s > 0$  like in Fig. 1(b), which supports left-moving worldlines in imaginary time. If we implement a boundary condition that affects its left-moving behavior, this piece of the spectrum, along with its BZ segment, will deviate from its PBC counterpart. The OBCs is one possibility, and another is a right-permissible (RP) CBCs, a unidirectional version of OBCs, where the leftward-permissible (LP) hopping across the boundary is completely suppressed [Fig. 1(c)]—it evaporates  $W_s$  and  $\text{Im}(\bar{v})$  and collapses the corresponding spectrum and BZ segment onto its OBC spectrum and GBZ counterpart; at the same time, their eigenstates will manifest the left-localized NHSE, as on top of the OBCs, the additional RP hopping poses little impact on the left-localized skin modes; unlike the OBCs, on the other hand,  $W_s < 0$  is compatible with the RP CBCs, and the related spectrum and BZ segments remains intact, and their eigenstates remain extended [53]. Analogously, vice versa for the LP CBCs.

Importantly, the intersections between the PBC BZ and the OBC GBZ, known as the Bloch points, mark the boundaries between segments with winding numbers of opposite signs; also, they separate the right-localized and left-localized skin modes under OBCs. Specifically, for a single-band model  $H(z) = \epsilon_z$  with  $z \in \text{BZ}$ , the winding number in Eq. (3) equals  $W_s = \mathcal{N}_0 - \mathcal{N}_p$ , where  $\mathcal{N}_0$  and  $\mathcal{N}_p$  are the number of the zeros and poles of  $H(z) - \epsilon_0$  inside the BZ, respectively. Given a right-hopping range of  $q$ , thus  $q$ -fold pole at  $z = 0$ , and whether  $\epsilon_0$  lies on the OBC spectrum associated with the GBZ segment inside or outside the BZ,  $\mathcal{N}_0$  is either  $q+1$  or  $q-1$  and thus  $W_s$  is either positive or negative. This conclusion follows from the GBZ condition, which mandates that the zeros with the  $q^{\text{th}}$  and  $(q+1)^{\text{th}}$  largest modulus lie on the GBZ [13] for a common 2-bifurcation point on OBC spectrum [82], yet generalizable to arbitrary  $n$ -bifurcation points or even systems with multiple bands. On the complex energy plane, these Bloch points separate the inside and outside segments of the GBZ and guarantee degeneracy between the PBC and OBC spectra [83]. Under the CBCs, the Bloch points serve as junctions, allowing for smooth switches between the PBC and OBC segments, simultaneously on the spectrum and the BZ/GBZ, as we will later discuss and demonstrate in the examples.

Furthermore, we can enhance our control by applying additional transformations that modify the relative standings between the BZ and GBZ, including similarity transformations and, more broadly, holomorphic mappings. In the following, we will demonstrate such formalism on several model examples.

*A paradigmatic model.*— To demonstrate winding control, we consider the following 1D single-band non-

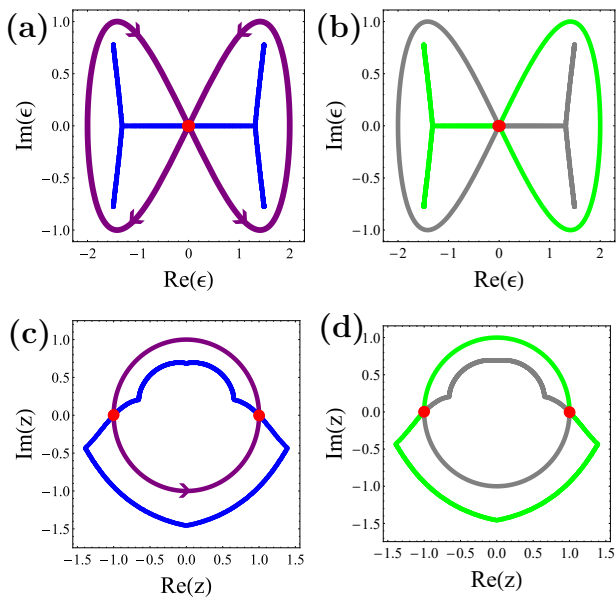


FIG. 2. The model in Eq. (4) serves as a typical example of winding-control spectrum and GBZ'. The (a) spectrum and (c) BZ under PBCs (purple) evolves to the spectrum and GBZ under OBCs (blue). In comparison, under the LP or RP CBC, the (b) spectrum and (d) GBZ' become a composite of certain PBC and OBC pieces, as the green or gray curves, respectively. The arrows indicate the spectral loops under PBCs, enclosing a positive (negative) winding number  $W_s$  region on the right (left) side. The red dots denote the Bloch points.

Hermitian model:

$$\hat{H}_p = \sum_x \left[ i(c_{x+1}^\dagger c_x - c_x^\dagger c_{x+1}) + \frac{1}{2}(c_{x+2}^\dagger c_x - c_x^\dagger c_{x+2}) \right] + \lambda_R \left[ ic_1^\dagger c_L + \frac{1}{2}(c_1^\dagger c_{L-1} + c_2^\dagger c_L) \right] - \lambda_L \left[ ic_L^\dagger c_1 + \frac{1}{2}(c_{L-1}^\dagger c_1 + c_L^\dagger c_2) \right], \quad (4)$$

where  $c_x$  ( $c_x^\dagger$ ) denotes the fermion annihilation (creation) operator at site  $x \in [1, L]$ , and  $\lambda_L, \lambda_R \in [0, 1]$  parametrize the left and right bound hopping between the boundaries, respectively. The PBC corresponds to  $\lambda_L = \lambda_R = 1$ , where the BZ is simply the unit circle in the complex plane [purple in Fig. 2(c)], and the spectrum  $H_p(z) = i(z^{-1} - z) + 1/2(z^{-2} - z^2)$ ,  $z \in \text{BZ}$  traces a self-intersecting loop in the complex energy plane [purple in Fig. 2(a)]. For  $\lambda_L = \lambda_R = 0$ , on the other hand, the OBC and its corresponding GBZ [blue arc in Fig. 2(c)] take effect. Indeed, the resulting spectrum  $H_p(z)$ ,  $z \in \text{GBZ}$  [blue arc in Fig. 2(a)] expels any simple loops and stands doubly degenerate in general. The BZ and GBZ intersect at two Bloch points [red dots in Fig. 2(c)], which precisely separate the parts clinging to left-localized NHSE (GBZ inside BZ) and right-localized NHSE (GBZ outside BZ); consistently [84], these Bloch points also correspond

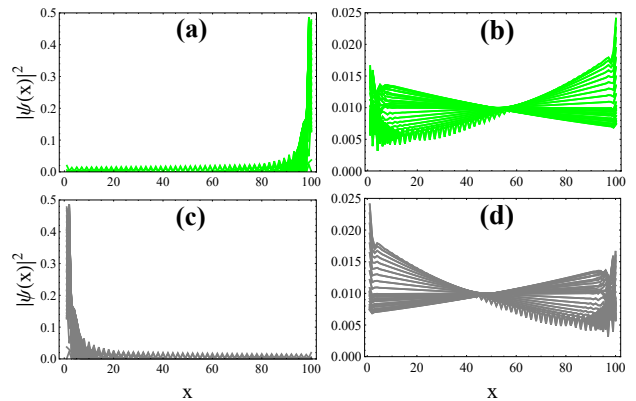


FIG. 3. Under LP CBC, (a) the eigenstates resembling the OBC spectrum and GBZ display right-localized NHSE, while (b) the eigenstates resembling the PBC spectrum and BZ show extended behaviors; see the green pieces in Fig. 2. Likewise, under RP CBC, (c) the eigenstates representing the OBC spectrum and GBZ display left-localized NHSE, while (d) the eigenstates representing the PBC spectrum and BZ show extended behaviors; see the gray pieces in Fig. 2.

to the self-intersection point of the PBC spectrum, partitioning segments with positive and negative winding number  $W_s$ .

Now, we impose the LP CBCs  $\lambda_L = 1$  and  $\lambda_R = 0$ , which turn off right-bound hopping across the boundary and block right-moving quasiparticles from circulating the 1D chain. This constraint in winding number influences the BZ and spectrum, but only the segments with negative winding numbers  $W_s$ —the left segment of the PBC spectrum collapses into the OBC spectrum [green curves in Fig. 2(b)], while the right segment remains intact; their respective (upper portion of) BZ and (lower portion of) GBZ merge at the Bloch points into a composite GBZ' [green loop in Fig. 2(d)]. Likewise, by imposing the RP CBCs with  $\lambda_L = 0$  and  $\lambda_R = 1$ , a non-positiveness requirement is enforced upon the winding number  $W_s$ , resulting in a combined spectrum and GBZ' as (gray curves in Fig. 2) as joining the respective PBC and OBC segments.

Further, we illustrate the eigenstate distributions in Fig. 3. When the right-bound (left-bound) hopping is turned off at the boundary with the LP (RP) CBCs, right-localized (left-localized) NHSE emerges; see Fig. 3(a) [Fig. 3(c)]; these eigenstates correspond to the portions of spectrum and GBZ' inherited from the OBC counterparts. In contrast, the eigenstates associated with the PBC segments remain fully extended [Figs. 3(b) and (d)], as in translation-invariant systems under PBCs. Furthermore, we provide in the Supplementary Materials additional rigorous explanations of spectrum and eigenstate behaviors under CBCs, continuous interpolations between the PBC and CBC, and winding control of a model with three PBC spectral loops [80].

*Winding control with similarity transformation and holomorphic mapping.*— The above CBC exhibits lim-

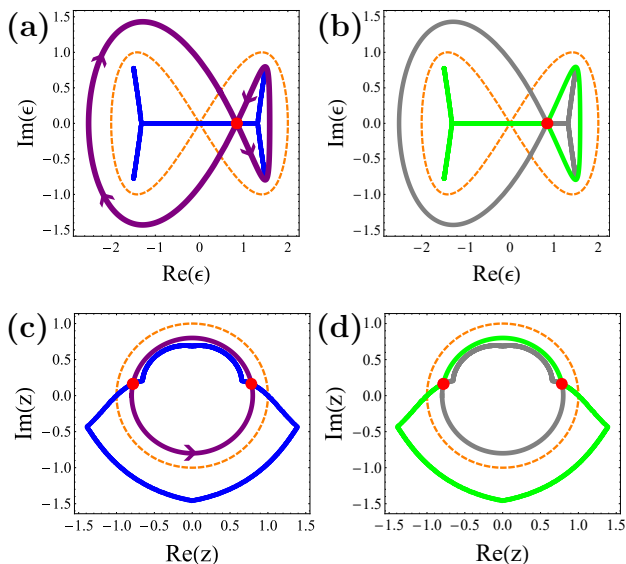


FIG. 4. The spectrum and GBZ (BZ) of the model in Eq. (4) following a similarity transformation with  $\varrho = 0.8$  showcase (a) an identical OBC spectrum and (b) GBZ to the original model as in Fig. 2, yet (a) a modified PBC spectrum, effectively according to (b) a transformed BZ—the circle of radius  $\varrho = 0.8$ . The original PBC spectrum and BZ (with  $\varrho = 1$ ) are shown as the orange dashed loops for comparison. Similar to Fig. 2, with the LP (green) or RP (gray) CBC, the (b) spectrum and (d) GBZ become a composite of certain PBC and OBC pieces. Note that varying  $\varrho$  changes the BZ and, thus, the location of the Bloch points.

itations in that it solely controls the keep or toss of sections between existing Bloch points. To achieve further control over the existence and location of the Bloch points, we employ a similarity transformation in conjunction with the CBCs. For simplicity, let us first consider  $H_{p,\varrho} = S^{-1}H_p S$ , where  $S = \text{diag}\{1, \varrho, \dots, \varrho^L\}$  and  $\varrho \in (0, +\infty)$ , which is trivial for OBC spectrum. However, with  $\lambda_L = \lambda_R = 1$  as before, the PBC spectrum  $H_p(z)$  follows a transformed BZ, a circle of radius  $\varrho$  in the complex plane. The Bloch points, the intersections between the OBC and PBC spectra, also displace depending on  $\varrho$ ; see Fig. 4 for illustrations [85].

With CBC implemented, the PBC spectral loops with the positive or negative winding number  $W_s$  (purple), or the OBC spectral lines with zero  $W_s$  (blue), located to the right or left of the Bloch point (red dot), along with the corresponding (transformed) BZ and GBZ, can be selectively chosen and combined in a manner analogous to the case in Eq. (4); see Figs. 4(b) and (d). Accordingly, the CBC eigenstates exhibit distinct skin effects or extended behaviors similar to Fig. 3, depending on their position relative to the Bloch points as governed by the winding-control mechanism.

Beyond the specific similarity transformation discussed above, we can extend our framework to more general holomorphic mappings  $\mathcal{F}$ , which cast the original unit-

circle BZ to  $\mathcal{F}[\text{BZ}]$  in the complex plane [86]. Equally, the effect of  $\mathcal{F}$  on the original lattice model Hamiltonian  $\mathcal{H}$  is obtainable from its transformation on the model's characteristic polynomial  $H(z) \rightarrow H(\mathcal{F}(z))$ . For example, the similarity transformation  $S$  is a straightforward holomorphic mapping  $\mathcal{F}(z) = \varrho z$ , which results in a contraction or dilatation of the BZ along the radial direction as in Fig. 4. Importantly, additional constraints are necessary to ensure the physical meaning of such a holomorphic mapping; for simplicity, we require that  $\mathcal{F}[\text{BZ}]$  remains a single loop and consider case-specific constraints as appropriate.

Next, we consider another holomorphic mapping  $\mathcal{F}'(z) = z - \eta$ ,  $\eta \in \mathbb{C}$  which translate the BZ to  $\mathcal{F}'[\text{BZ}]$  via a displacement of  $\eta$ . For example, the non-Bloch Hamiltonian of the Hatano-Nelson (HN) model is  $H_{HN}(z) = (1 + \gamma)z + (1 - \gamma)z^{-1}$  [12, 87, 88], yielding the PBC and OBC spectra [orange dashed loop and magenta solid line in Fig. 5(a)] following  $z \in \text{BZ}$  and  $z \in \text{GBZ}$  [orange dashed and magenta solid loops in Fig. 5(b)], respectively. Further,  $\mathcal{F}'$  with  $\eta = 0.45$  shifts the original BZ to  $\mathcal{F}'[\text{BZ}]$  as the purple loop, which now intersects the OBC GBZ (magenta loop) at two emergent Bloch points (red dots) as in Fig. 5(b). According to  $z \in \mathcal{F}'[\text{BZ}]$ , the PBC spectrum  $H_{HN}(z)$  transforms into two loops with opposite winding numbers demarcated by the Bloch point [purple curves and red dots in Fig. 5(a)]. Nevertheless, we expect the OBC spectrum to remain mainly invariant following the holomorphic mapping. In analogy with the previous examples, we may introduce further winding control via LP or RP CBCs. The LP (RP) CBC should impose a  $W_s > 0$  ( $W_s < 0$ ) constraint and collapse the right (left) loop with  $W_s < 0$  ( $W_s > 0$ ) from the transformed PBC spectrum onto its OBC counterpart, while the left (right) loop with  $W_s > 0$  ( $W_s < 0$ ) remains intact; their GBZ' should also combine the corresponding BZ and GBZ pieces between the Bloch points.

In practice, following the effect of  $\mathcal{F}'$  on the characteristic equation  $H_{HN}(z)$ , we transform the original HN model into the following tight-binding lattice model:

$$\hat{H}' = \sum_x \left[ (1 + \gamma)c_x^\dagger c_{x+1} - \eta c_x^\dagger c_x + (1 - \gamma) \sum_{n=0}^{\infty} \eta^n c_{x+n}^\dagger c_{x-1} \right], \quad (5)$$

where we have essentially expanded  $H_{HN}(z - \eta)$  in Laurent series, which remains valid when  $|\eta/z| < 1$  for all  $z \in \mathcal{F}'[\text{BZ}]$ . We take  $\eta = 0.45$  and truncate the hopping range  $n$  at a sufficient  $n_{max} = 20$ , and summarize the results in Fig. 5.

Under OBCs, the transformed model yields a spectrum, represented by the blue points in Fig. 5(a), which provides a good approximation of the original OBC spectrum (magenta solid line) [89]. Also, its PBC spectrum's consistency with our theoretical expectation is self-evident from the  $H_{HN}(z - \eta)$  nature of Eq. (5). Further, as we employ CBCs for the transformed model, the resulting spectra and eigenstates combine the corresponding pieces from the transformed PBC and OBC

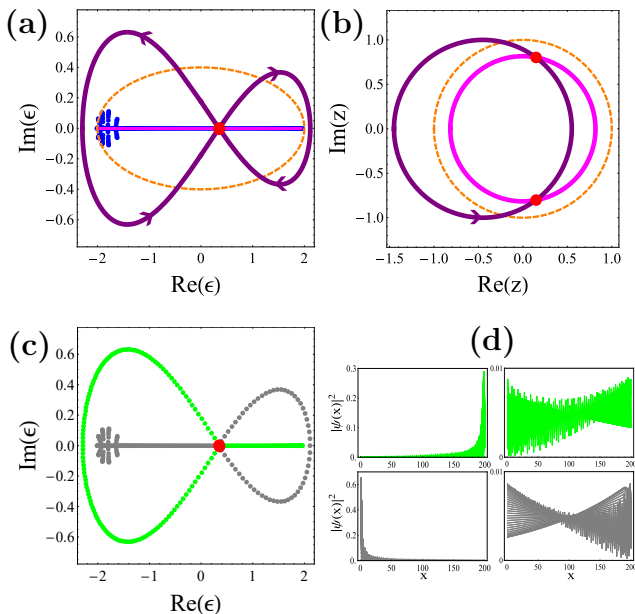


FIG. 5. The spectrum and GBZ (BZ) of the HN models showcase the winding control we possess with a holomorphic mapping  $\mathcal{F}'(z) = z - \eta$  and CBC. (a) the OBC (magenta, blue) and PBC (orange, purple) spectra of the original (magenta, orange) and transformed (blue, purple) HN models consistently follow their corresponding PBC BZ (orange), transformed BZ (purple), and OBC GBZ (magenta) in (b). Together with the LP (green) and RP (gray) CBCs, the (c) spectra and (d) eigenstates of the transformed model follow the winding-control mechanism, combining features (winding number  $W_s$ , skin effects or extended wave functions) of the respective pieces of OBC and transformed PBC between the Bloch points (red dots), as we demonstrated in the previous examples. We set  $\eta = 0.45$ ,  $\gamma = 0.2$ , and truncation  $n_{max} = 20$  on a 1D chain with  $L = 200$  sites.

spectra and eigenstates [Figs. 5(c) and (d)] as we have argued in the previous paragraphs. Therefore, we have

demonstrated that we can obtain further control and design over the spectrum and GBZ through winding-control boundary conditions and general holomorphic mappings, and we may incorporate other holomorphic mappings for further control targets.

*Conclusions.*— In summary, we have proposed and explored a winding-control mechanism rooted in the interplay between the spectral winding number, the imaginary velocity, and the boundary conditions. With CBCs of unilateral boundary hoppings, we selectively combine segments of PBC and OBC spectra as well as corresponding BZ and GBZ, separated by Bloch points and dictated by their winding characteristics. As a result, the localization behaviors of the eigenstates are determined not by individual BZ or GBZ but instead from their combined intersections under boundary control. Additionally, similarity transformations or holomorphic mappings extend this control, providing a versatile and systematic framework for manipulating non-Hermitian spectral topology. We have validated this winding control through various 1D lattice model examples.

Our winding-control mechanism also holds broader application potential beyond CBCs. For example, by joining different models, such as the HN model and the non-Hermitian Su-Schrieffer-Heeger model, the winding control can hybridize their spectra [80]. Furthermore, cases with multiple bands provide sublattice/spin-dependent or summation-based CBC generalizations of the aforementioned scenarios. Notably, the imaginary velocity and worldline winding numbers remain physical in quantum many-body representations, validating many-body extensions of winding control and CBCs into interacting systems beyond single-particle spectra and GBZs, an interesting topic for future studies.

*Acknowledgment.*— Y.F. is supported by a startup grant from Zhejiang Normal University. Y.Z. is supported by the National Natural Science Foundation of China (Grants No.92270102 & No.12174008) and the National Key R&D Program of China (Grant No.2022YFA1403700).

- 
- [1] A. Yuto, G. Zongping, and U. Masahito, *Advances in Physics* **69**, 249 (2020).
  - [2] E. J. Bergholtz, J. C. Budich, and F. K. Kunst, *Rev. Mod. Phys.* **93**, 015005 (2021).
  - [3] T. E. Lee, *Phys. Rev. Lett.* **116**, 133903 (2016).
  - [4] D. Leykam, K. Y. Bliokh, C. Huang, Y. D. Chong, and F. Nori, *Phys. Rev. Lett.* **118**, 040401 (2017).
  - [5] V. M. Martinez Alvarez, J. E. Barrios Vargas, and L. E. F. Foa Torres, *Phys. Rev. B* **97**, 121401 (2018).
  - [6] H. Shen, B. Zhen, and L. Fu, *Phys. Rev. Lett.* **120**, 146402 (2018).
  - [7] Z. Gong, Y. Ashida, K. Kawabata, K. Takasan, S. Higashikawa, and M. Ueda, *Phys. Rev. X* **8**, 031079 (2018).
  - [8] K. Kawabata, K. Shiozaki, M. Ueda, and M. Sato, *Phys. Rev. X* **9**, 041015 (2019).
  - [9] F. K. Kunst, E. Edvardsson, J. C. Budich, and E. J. Bergholtz, *Phys. Rev. Lett.* **121**, 026808 (2018).
  - [10] S. Yao and Z. Wang, *Phys. Rev. Lett.* **121**, 086803 (2018).
  - [11] S. Yao, F. Song, and Z. Wang, *Phys. Rev. Lett.* **121**, 136802 (2018).
  - [12] K. Yokomizo and S. Murakami, *Phys. Rev. Lett.* **123**, 066404 (2019).
  - [13] K. Zhang, Z. Yang, and C. Fang, *Phys. Rev. Lett.* **125**, 126402 (2020).
  - [14] D. S. Borgnia, A. J. Kruchkov, and R.-J. Slager, *Phys. Rev. Lett.* **124**, 056802 (2020).
  - [15] Z. Yang, K. Zhang, C. Fang, and J. Hu, *Phys. Rev. Lett.* **125**, 226402 (2020).
  - [16] N. Okuma, K. Kawabata, K. Shiozaki, and M. Sato, *Phys. Rev. Lett.* **124**, 086801 (2020).
  - [17] H.-Y. Wang, F. Song, and Z. Wang, *Phys. Rev. X* **14**, 021011 (2024).

- [18] C. H. Lee, L. Li, and J. Gong, *Phys. Rev. Lett.* **123**, 016805 (2019).
- [19] K. Kawabata, M. Sato, and K. Shiozaki, *Phys. Rev. B* **102**, 205118 (2020).
- [20] R. Okugawa, R. Takahashi, and K. Yokomizo, *Phys. Rev. B* **102**, 241202 (2020).
- [21] Y. Fu, J. Hu, and S. Wan, *Phys. Rev. B* **103**, 045420 (2021).
- [22] H. Hu and E. Zhao, *Phys. Rev. Lett.* **126**, 010401 (2021).
- [23] Y. Li, X. Ji, Y. Chen, X. Yan, and X. Yang, *Phys. Rev. B* **106**, 195425 (2022).
- [24] Y. Fu and Y. Zhang, *Phys. Rev. B* **110**, L121401 (2024).
- [25] X. Ji, H. Geng, N. Akhtar, and X. Yang, *Phys. Rev. B* **111**, 195419 (2025).
- [26] F. Song, S. Yao, and Z. Wang, *Phys. Rev. Lett.* **123**, 170401 (2019).
- [27] A. McDonald, R. Hanai, and A. A. Clerk, *Phys. Rev. B* **105**, 064302 (2022).
- [28] A. Altland, M. Fleischhauer, and S. Diehl, *Phys. Rev. X* **11**, 021037 (2021).
- [29] A. Gómez-León, T. Ramos, A. González-Tudela, and D. Porras, *Phys. Rev. A* **106**, L011501 (2022).
- [30] B. Li, H.-R. Wang, F. Song, and Z. Wang, *Phys. Rev. B* **109**, L201121 (2024).
- [31] A. Guo, G. J. Salamo, D. Duchesne, R. Morandotti, M. Volatier-Ravat, V. Aimez, G. A. Siviloglou, and D. N. Christodoulides, *Phys. Rev. Lett.* **103**, 093902 (2009).
- [32] W. Chen, Ş. Kaya Özdemir, G. Zhao, J. Wiersig, and L. Yang, *Nature* **548**, 192 (2017).
- [33] L. Xiao, K. Wang, X. Zhan, Z. Bian, K. Kawabata, M. Ueda, W. Yi, and P. Xue, *Phys. Rev. Lett.* **123**, 230401 (2019).
- [34] L. Xiao, T. Deng, K. Wang, G. Zhu, Z. Wang, W. Yi, and P. Xue, *Nature Physics* **16**, 761 (2020).
- [35] L. Xiao, T. Deng, K. Wang, Z. Wang, W. Yi, and P. Xue, *Phys. Rev. Lett.* **126**, 230402 (2021).
- [36] L. Xiao, W.-T. Xue, F. Song, Y.-M. Hu, W. Yi, Z. Wang, and P. Xue, *Phys. Rev. Lett.* **133**, 070801 (2024).
- [37] M. Ezawa, *Phys. Rev. B* **99**, 121411 (2019).
- [38] M. Ezawa, *Phys. Rev. B* **100**, 081401 (2019).
- [39] T. Hofmann, T. Helbig, F. Schindler, N. Salgo, M. Brzezińska, M. Greiter, T. Kiessling, D. Wolf, A. Vollhardt, A. Kabaši, C. H. Lee, A. Bilušić, R. Thomale, and T. Neupert, *Phys. Rev. Res.* **2**, 023265 (2020).
- [40] T. Helbig, T. Hofmann, S. Imhof, M. Abdelghany, T. Kiessling, L. W. Molenkamp, C. H. Lee, A. Szameit, M. Greiter, and R. Thomale, *Nature Physics* **16**, 747 (2020).
- [41] L. Li, C. H. Lee, and J. Gong, *Communications Physics* **4**, 42 (2021).
- [42] M. Brandenbourger, X. Locsin, E. Lerner, and C. Coulais, *Nature Communications* **10**, 4608 (2019).
- [43] A. Ghatak, M. Brandenbourger, J. van Wezel, and C. Coulais, *Proceedings of the National Academy of Sciences* **117**, 29561 (2020).
- [44] Y. Chen, X. Li, C. Scheibner, V. Vitelli, and G. Huang, *Nature Communications* **12**, 5935 (2021).
- [45] W. Wang, X. Wang, and G. Ma, *Nature* **608**, 50 (2022).
- [46] W. Wang, M. Hu, X. Wang, G. Ma, and K. Ding, *Phys. Rev. Lett.* **131**, 207201 (2023).
- [47] Z. Li, L.-W. Wang, X. Wang, Z.-K. Lin, G. Ma, and J.-H. Jiang, *Nature Communications* **15**, 6544 (2024).
- [48] R. Hamazaki, K. Kawabata, and M. Ueda, *Phys. Rev. Lett.* **123**, 090603 (2019).
- [49] L.-Z. Tang, L.-F. Zhang, G.-Q. Zhang, and D.-W. Zhang, *Phys. Rev. A* **101**, 063612 (2020).
- [50] S. Schiffer, X.-J. Liu, H. Hu, and J. Wang, *Phys. Rev. A* **103**, L011302 (2021).
- [51] Y. Liu, Q. Zhou, and S. Chen, *Phys. Rev. B* **104**, 024201 (2021).
- [52] K. Kawabata and S. Ryu, *Phys. Rev. Lett.* **126**, 166801 (2021).
- [53] S.-X. Hu, Y.-X. Fu, and Y. Zhang, *Residue imaginary velocity induces many-body delocalization* (2024), arXiv:2407.15954 [quant-ph].
- [54] E. Lee, H. Lee, and B.-J. Yang, *Phys. Rev. B* **101**, 121109 (2020).
- [55] S. Mu, C. H. Lee, L. Li, and J. Gong, *Phys. Rev. B* **102**, 081115 (2020).
- [56] P.-Y. Chang, J.-S. You, X. Wen, and S. Ryu, *Phys. Rev. Res.* **2**, 033069 (2020).
- [57] R. Shen and C. H. Lee, *Communications Physics* **5**, 238 (2022).
- [58] S.-B. Zhang, M. M. Denner, T. c. v. Bzdušek, M. A. Sentef, and T. Neupert, *Phys. Rev. B* **106**, L121102 (2022).
- [59] N. Matsumoto, K. Kawabata, Y. Ashida, S. Furukawa, and M. Ueda, *Phys. Rev. Lett.* **125**, 260601 (2020).
- [60] F. Alsallom, L. Herviou, O. V. Yazyev, and M. Brzezińska, *Phys. Rev. Res.* **4**, 033122 (2022).
- [61] K. Kawabata, T. Numasawa, and S. Ryu, *Phys. Rev. X* **13**, 021007 (2023).
- [62] T. Haga, M. Nakagawa, R. Hamazaki, and M. Ueda, *Phys. Rev. Lett.* **127**, 070402 (2021).
- [63] F. Yang, Q.-D. Jiang, and E. J. Bergholtz, *Phys. Rev. Res.* **4**, 023160 (2022).
- [64] S. Guo, C. Dong, F. Zhang, J. Hu, and Z. Yang, *Phys. Rev. A* **106**, L061302 (2022).
- [65] H. Li and S. Wan, *Phys. Rev. B* **106**, L241112 (2022).
- [66] K. Shimomura and M. Sato, *Phys. Rev. Lett.* **133**, 136502 (2024).
- [67] R. Shen, F. Qin, J.-Y. Desaulles, Z. Papić, and C. H. Lee, *Phys. Rev. Lett.* **133**, 216601 (2024).
- [68] J. Gliozzi, G. De Tomasi, and T. L. Hughes, *Phys. Rev. Lett.* **133**, 136503 (2024).
- [69] Y.-M. Hu, Z. Wang, B. Lian, and Z. Wang, *Many-body non-hermitian skin effect with exact steady states in dissipative lattice gauge theory* (2025), arXiv:2502.03534 [quant-ph].
- [70] J. Gliozzi, F. Balducci, T. L. Hughes, and G. D. Tomasi, *Non-hermitian multipole skin effects challenge localization* (2025), arXiv:2504.10580 [cond-mat.dis-nn].
- [71] C.-X. Guo, C.-H. Liu, X.-M. Zhao, Y. Liu, and S. Chen, *Phys. Rev. Lett.* **127**, 116801 (2021).
- [72] P. Mognini, O. Arandes, and E. J. Bergholtz, *Phys. Rev. Res.* **5**, 033058 (2023).
- [73] C.-X. Guo, X. Wang, H. Hu, and S. Chen, *Phys. Rev. B* **107**, 134121 (2023).
- [74] Y. Fu and Y. Zhang, *Phys. Rev. B* **108**, 205423 (2023).
- [75] B. Li, H.-R. Wang, F. Song, and Z. Wang, *Phys. Rev. B* **108**, L161409 (2023).
- [76] Throughout the paper, we adopt a unified notation convention for the Hamiltonians. The symbol with a hat,  $\hat{H}$ , explicitly denotes the Hamiltonian operator in the second-quantized formalism. In contrast, the symbol without a hat,  $H$ , refers to the Hamiltonian matrix under OBCs, with boundary hoppings excluded. Meanwhile,  $H(z)$  represents the so-called non-Bloch Hamilto-

nian, obtained by analytically continuing the momentum-space Hamiltonian  $H(k)$ ,  $k \in \text{BZ}$  (defined under PBCs) through the mapping  $e^{ik} \rightarrow z \in \mathbb{C}$ .

- [77] This filling convention can be generalized to filled (empty) states with  $\text{Re}(e^{i\theta}\epsilon) < \mu$  [ $\text{Re}(e^{i\theta}\epsilon) > \mu$ ] via a mapping  $\hat{H}' = \hat{H}e^{i\theta} - \mu\hat{N}$ , where  $\hat{N}$  is the fermion number operator, e.g., the Fermi sea  $\text{Im}(\epsilon) > 0$  in terms of long-time steady-state dynamics [53].
- [78] Multiple bands, if exist, need to be summed over.
- [79] S.-X. Hu, Y. Fu, and Y. Zhang, *Phys. Rev. B* **108**, 245114 (2023).
- [80] See the supplementary materials for further details.
- [81] K. Zhang, Z. Yang, and C. Fang, *Nature Communications* **13**, 2496 (2022).
- [82] An energy on the OBC spectrum that corresponds to  $n$  distinct points on the GBZ is referred to as an  $n$ -bifurcation point [84].
- [83] Without loss of clarity, we hereafter refer to such interactions on both the BZ/GBZ and the spectra as Bloch points.
- [84] D. Wu, J. Xie, Y. Zhou, and J. An, *Phys. Rev. B* **105**, 045422 (2022).
- [85] Equivalently, one can obtain the PBC spectrum  $H_{p,\rho}(z)$  by evaluating it on standard BZ (unit circle), and the corresponding OBC spectrum by applying the transformed GBZ associated with  $H_{p,\rho}$ . Both schemes yield identical PBC and OBC spectra. In Fig. 4, we have adopted the former approach.
- [86] Here and below, we denote  $\mathcal{F}(z)$  and  $\mathcal{F}[\text{BZ}]$  as the images of the element  $z$  and the set BZ under the mapping  $\mathcal{F}$ , respectively.
- [87] N. Hatano and D. R. Nelson, *Phys. Rev. Lett.* **77**, 570 (1996).
- [88] N. Hatano and D. R. Nelson, *Phys. Rev. B* **56**, 8651 (1997).
- [89] The truncation mainly influences the far-left edge of the OBC spectrum, leaving multiple protruding branches, but does not change the winding-control mechanism. A larger truncation  $n_{max}$  allows a better approximation to the model and spectrum in Eq. (5).

## Supplementary Materials for “Winding-Control Mechanism of Non-Hermitian Systems”

### I. OPEN-BOUNDARY SPECTRA AND THE VANISHING OF VELOCITY

The open boundary conditions (OBCs) ensures the worldline winding number  $W$  thus the velocity  $\bar{v}$  vanishes [53, 79], and the intercepts of the spectrum with the imaginary axis (Fermi surface at  $\text{Re} E = 0$ ) always coincide, irrespective of the change of Fermi energy  $\mu$  and the phase angle  $\theta$  (in  $\hat{H}' = \hat{H}e^{i\theta} - \mu\hat{N}$ ), which shifts and rotates the real and imaginary axes in the energy plane. This guarantees that the (back-and-forth) energy levels are doubly encountered, or we will always be able to find a reference frame  $(\mu, \theta)$  that separates these two levels and ends up a nonzero  $\bar{v}$ , violating the OBC prerequisite.

Detailedly and technically, the OBC spectra of a non-Hermitian system corresponds to the generalized Brillouin zone (GBZ)-condition  $|z_1| \leq \dots \leq |z_M| = |z_{M+1}| \leq \dots \leq |z_{2M}|$ , where  $z$ 's are the norm-ordered roots (assume  $2M$ ) of the characteristic equation  $\det[H(z) - E] = 0$  with the non-Bloch Hamiltonian of the system [10, 12]. An energy  $E_0$  with  $n$   $z$ 's values on (sub-)GBZ is  $n$ -bifurcation point [84].

For the single-band case, the 1-bifurcation points correspond to the endpoints of the spectrum, while the 2-bifurcation points are common on the OBC spectrum, smoothly connecting in the thermodynamic limit to form a continuous segment. For  $n$ -bifurcation points ( $n > 2$ ), these represent the intersections of several smooth 2-bifurcation segments and manifest as cusps on the spectrum and GBZ. As a simple example, when the Fermi surface  $E_F = \mu$  in the complex plane intersects a single 2-bifurcation point of a single band (as shown in Fig. 6(a), using the paradigmatic model in the main text), the two-visit rule (back-and-forth motion) as the argument  $k$  of the GBZ evolves guarantees the corresponding velocity vanishes, as shown in Fig. 6(c). This is expressed by the equation

$$\bar{v} = \sum_{\text{Re}(\epsilon_k) < \mu} v_k = \frac{L}{2\pi} \int_{k_{F,1}}^{k_{F,2}} \frac{\partial \epsilon_k}{\partial k} dk = \frac{L}{2\pi} (\epsilon_F - \epsilon_F) = 0, \quad (6)$$

where the integral corresponds to the continuous band in the thermodynamic limit, and the orange arrow in Fig. 6(c) indicates the evolution of  $k$  (the argument of  $z$  on the GBZ). In the case where the Fermi surface  $E_F = \mu$  intersects two 2-bifurcation points [Figs. 6(b) and (d)], the corresponding velocity still vanishes,

$$\bar{v} = \sum_{\text{Re}(\epsilon_k) < \mu} v_k = \frac{L}{2\pi} \left( \int_{k_{F,1}^d}^{k_{F,2}^d} + \int_{k_{F,1}^u}^{k_{F,2}^u} \right) \frac{\partial \epsilon_k}{\partial k} dk = \frac{L}{2\pi} [(\epsilon_F^d - \epsilon_F^d) + (\epsilon_F^u - \epsilon_F^u)] = 0. \quad (7)$$

Thus, the OBC nature enforces the vanishing of the single-band velocity  $\bar{v} = 0$  for any Fermi-surface configuration. The key point here is that the starting and ending Fermi points in the integration (such as in Eqs. (6) and (7)) always

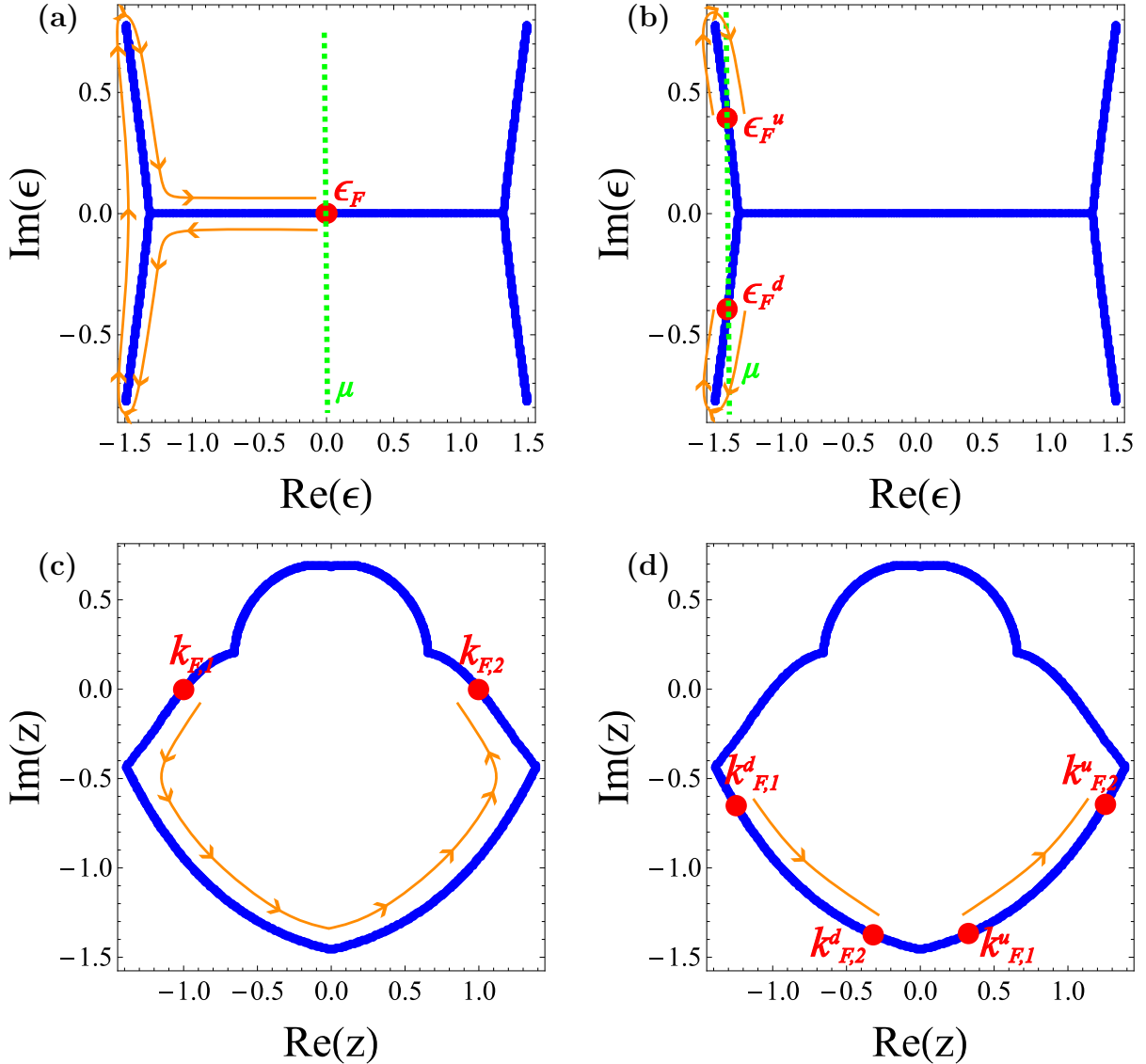


FIG. 6. Illustration of the vanishing of  $\text{Im}(\bar{v})$  for the single OBC band, using the paradigmatic model in the main text. Assuming the Fermi surface  $E_F = \mu$  (Green dashed lines), it intersects the OBC spectrum at single and two Fermi points (Red points) in panels (a) and (c), respectively. The corresponding  $k$ -evolutions on the GBZ are shown in panels (c) and (d), where the orange arrows indicate the flow directions.

coincide, reflecting the back-and-forth property inherent in the OBC spectrum. This is the exact manifestation of the double degeneracy.

For the multi-band cases, the OBC nature constraints the vanishing of the total velocity  $\bar{v}$ , which is the summation of the velocities for all bands  $\bar{v} = \sum_{\alpha} \bar{v}^{\alpha}$ ,

$$\bar{v}^{\alpha} = \sum_{\text{Re}(\epsilon_k^{\alpha}) < \mu} v_k^{\alpha}, \quad (8)$$

where  $k$  corresponds to the argument of  $z$  on the sub-GBZ  $\mathcal{C}_{\alpha}$ . While the velocity  $\bar{v}^{\alpha}$  of an individual band may not necessarily vanish (depending on the configuration of the spectrum and the Fermi-surface settings), the total velocity  $\bar{v}$  must vanish under OBCs. The double degeneracy (back-and-forth) may be borne by one or more OBC bands. The above statement is essentially consistent with the total persistent current analysis presented in Ref. [13].

## II. DERIVATION OF THE SPECTRUM AND EIGENSTATE LOCALIZATION UNDER CBCS

In this section, we investigate the localized conditional boundary condition (CBC) eigenstates of the paradigmatic model detailly in the main text, which generally reads

$$\hat{H} = \sum_x \left[ t_L c_x^\dagger c_{x+1} + t_R c_{x+1}^\dagger c_x + \gamma_L c_x^\dagger c_{x+2} + \gamma_R c_{x+2}^\dagger c_x + \lambda_R \left( t_R c_1^\dagger c_L + \gamma_R c_1^\dagger c_{L-1} + \gamma_R c_2^\dagger c_L \right) \right. \\ \left. + \lambda_L \left( t_L c_L^\dagger c_1 + \gamma_L c_{L-1}^\dagger c_1 + \gamma_L c_L^\dagger c_2 \right) \right]. \quad (9)$$

Assuming the translation-invariant trail solution  $|\psi_t\rangle = \sum_x z^x |x\rangle$  or the matrix form  $\psi_t = (\psi_1, \dots, \psi_L)^T$ , we immediately obtain the equation with respect to energy  $E$  in the bulk

$$\gamma_R \psi_{x-2} + t_R \psi_{x-1} + t_L \psi_{x+1} + \gamma_L \psi_{x+2} = E \psi_x, \quad (10)$$

which gives the characteristic equation

$$H(z) - E = \frac{1}{z^2} (\gamma_L z^4 + t_L z^3 - E z^2 + t_R z + \gamma_R) = 0, \quad (11)$$

with  $H(z) = \gamma_L z^2 + t_L z + t_R z^{-1} + \gamma_R z^{-2}$ . The bulk equation produces general four  $z$  roots, denoting as  $|z_1| \leq |z_2| \leq |z_3| \leq |z_4|$ . The form of eigenstates reads  $|\Psi\rangle = \sum_{p=1}^4 a_p |\psi^{(p)}\rangle$  or the matrix form  $\Psi = (\Psi_1, \dots, \Psi_L)^T$  with  $|\psi^{(p)}\rangle = \sum_x z_p^x |x\rangle$ .

Before deriving the CBC solutions, we briefly review the periodic boundary condition (PBC) and OBC cases. The eigenstates at the left and right edges are constrained by the equations

$$t_L \Psi_2 + \gamma_L \Psi_3 + \gamma_R \Psi_{L-1} + t_R \Psi_L = E \Psi_1, \quad (12)$$

$$t_R \Psi_1 + t_L \Psi_3 + \gamma_L \Psi_4 + \gamma_R \Psi_L = E \Psi_2, \quad (13)$$

$$\gamma_L \Psi_1 + \gamma_R \Psi_{L-3} + t_R \Psi_{L-2} + t_L \Psi_L = E \Psi_{L-1}, \quad (14)$$

$$t_L \Psi_1 + \gamma_L \Psi_2 + \gamma_R \Psi_{L-2} + t_R \Psi_{L-1} = E \Psi_L, \quad (15)$$

when we adopt the PBCs  $(\lambda_R, \lambda_L) = (1, 1)$ . Substituting  $\Psi$  into these boundary equations, we obtain

$$\sum_{p=1}^4 (t_L z_p^2 + \gamma_L z_p^3 + \gamma_R z_p^{L-1} + t_R z_p^L - E z_p) a_p = 0, \quad (16)$$

$$\sum_{p=1}^4 (t_R z_p + t_L z_p^3 + \gamma_L z_p^4 + \gamma_R z_p^L - E z_p^2) a_p = 0, \quad (17)$$

$$\sum_{p=1}^4 (\gamma_L z_p + \gamma_R z_p^{L-3} + t_R z_p^{L-2} + t_L z_p^L - E z_p^{L-1}) a_p = 0, \quad (18)$$

$$\sum_{p=1}^4 (t_L z_p + \gamma_L z_p^2 + \gamma_R z_p^{L-2} + t_R z_p^{L-1} - E z_p^L) a_p = 0. \quad (19)$$

According to the well-known Bloch band theorem, the admissible solutions under PBCs require that one of the four  $z$ 's satisfies  $z_p = e^{i2\pi n/L}$  for  $n = 0, 1, \dots, L-1$ , with the corresponding coefficient  $a_p = 1$  and all others  $a_{j \neq p} = 0$ . The eigenenergies are given by  $H(z_p)$  and the full eigenstates are the plane-wave like Bloch states with uniform distributions, as commonly described in solid-state physics textbooks. When we break the periodicity at both two

edges, the OBCs impose the above boundary equations into

$$\sum_{p=1}^4 (t_L z_p^2 + \gamma_L z_p^3 - E z_p) a_p = 0, \quad (20)$$

$$\sum_{p=1}^4 (t_R z_p + t_L z_p^3 + \gamma_L z_p^4 - E z_p^2) a_p = 0, \quad (21)$$

$$\sum_{p=1}^4 (\gamma_R z_p^{L-3} + t_R z_p^{L-2} + t_L z_p^L - E z_p^{L-1}) a_p = 0, \quad (22)$$

$$\sum_{p=1}^4 (\gamma_R z_p^{L-2} + t_R z_p^{L-1} - E z_p^L) a_p = 0. \quad (23)$$

In the thermodynamic limit (i.e., for sufficiently large  $L$ ), the solutions are determined by the continuous band condition  $|z_2| = |z_3|$ , which defines the GBZ in the complex  $z$  plane [10, 12]. The OBC band is given by  $H(z)$ ,  $z \in \text{GBZ}$  and the corresponding eigenstates are non-Hermitian skin modes localized at one of the system's boundaries. Note that the PBC solutions are exact for any system size, whereas the GBZ-based OBC solutions are valid only in the thermodynamic limit, with finite-size effects becoming more significant for small  $L$  [74].

Now we consider the CBCs with  $(\lambda_R, \lambda_L) = (0, 1)$  allowing the left-moving quasiparticles. The boundary equations become

$$\sum_{p=1}^4 (t_L z_p^2 + \gamma_L z_p^3 - E z_p) a_p = 0, \quad (24)$$

$$\sum_{p=1}^4 (t_R z_p + t_L z_p^3 + \gamma_L z_p^4 - E z_p^2) a_p = 0, \quad (25)$$

$$\sum_{p=1}^4 (\gamma_L z_p + \gamma_R z_p^{L-3} + t_R z_p^{L-2} + t_L z_p^L - E z_p^{L-1}) a_p = 0, \quad (26)$$

$$\sum_{p=1}^4 (t_L z_p + \gamma_L z_p^2 + \gamma_R z_p^{L-2} + t_R z_p^{L-1} - E z_p^L) a_p = 0, \quad (27)$$

which gives the matrix equation

$$\mathcal{B} \cdot (a_1, a_2, a_3, a_4)^T = 0, \quad \mathcal{B} = \begin{pmatrix} T_1 & T_2 & T_3 & T_4 \\ S_1 & S_2 & S_3 & S_4 \\ U_1 + R_1 z_1^L & U_2 + R_2 z_2^L & U_3 + R_3 z_3^L & U_4 + R_4 z_4^L \\ V_1 + Q_1 z_1^L & V_2 + Q_2 z_2^L & V_3 + Q_3 z_3^L & V_4 + Q_4 z_4^L \end{pmatrix}, \quad (28)$$

with

$$t_L z_p^2 + \gamma_L z_p^3 - E z_p = T_p, \quad (29)$$

$$t_R z_p + t_L z_p^3 + \gamma_L z_p^4 - E z_p^2 = S_p, \quad (30)$$

$$\gamma_R z_p^{-3} + t_R z_p^{-2} + t_L - E z_p^{-1} = R_p, \quad (31)$$

$$\gamma_R z_p^{-2} + t_R z_p^{-1} - E = Q_p, \quad (32)$$

$$\gamma_L z_p = U_p, \quad (33)$$

$$t_L z_p + \gamma_L z_p^2 = V_p. \quad (34)$$

The existence of the solution  $(a_1, a_2, a_3, a_4)^T$  requires  $\det \mathcal{B} = 0$ , giving the following polynomial

$$\sum_{X,Y} \mathcal{F}(z_{k \in X}, z_{j \in Y}, E) \prod_{k \in X} z_k^L + \sum_{p=1}^4 \mathcal{G}(E) z_p^L + O(1) = 0, \quad (35)$$

where the sets  $X$  and  $Y$  are two disjoint subsets of the set  $\{1, 2, 3, 4\}$ . The analysis of the CBC solutions is divided into two cases for sufficiently large  $L$ : **(i)** all  $z$ 's satisfy  $|z| \neq 1$ , **(ii)** at least one  $z$  has unit modulus, i.e.,  $|z| = 1$ . The following analysis follows this case-based classification.

**(i)** This case includes the following possibilities:

(a)  $1 < |z_1| \leq |z_2| \leq |z_3| \leq |z_4|$  or  $|z_1| < 1 \leq |z_2| \leq |z_3| \leq |z_4|$ : In these scenarios, the two leading terms of Eq. (35) are associated with  $z_4^L z_2^L$  and  $z_4^L z_3^L$ . The cancellation condition between these two dominant terms gives rise precisely to the continuous band condition  $|z_2| = |z_3|$  with the GBZ portion whose modulus is greater than 1. This defines the GBZ segment with modulus greater than 1, which corresponds to part of the OBC spectrum in the thermodynamic limit. Further, the terms  $\gamma_L z_p$  in Eq. (26) and  $t_L z_p + \gamma_L z_p^2$  in Eq. (27) become negligible for  $|z_p| > 1$ . As a result, the skin modes governed by the condition  $1 < |z_2| = |z_3|$  along the GBZ segment, and the corresponding dominant coefficients  $a_2$  and  $a_3$  are consistent with those obtained under full OBCs.

(b)  $|z_1| \leq |z_2| < 1 < |z_3| \leq |z_4|$ ,  $|z_1| \leq |z_2| \leq |z_3| < 1 < |z_4|$ , or  $|z_1| \leq |z_2| \leq |z_3| \leq |z_4| < 1$ : In these scenarios, only a single leading term is allowed for each case—associated with either  $z_4^L z_3^L$ ,  $z_4^L$ , or  $O(1)$ , which is insufficient to give rise to a continuous band condition.

**(ii)** The second case indicates the presence of a segment of the PBC spectrum, corresponding to  $H(z)$ ,  $|z| = 1$ . While the PBC portion is presented in the main text, the opposite scenario illustrated by the green segment in Fig. 7, where the PBC spectral portion encloses the OBC spectral portion and the argument ranges of GBZ and BZ segments are identical, is prohibited. To show that such a configuration cannot occur, we proceed by contradiction. If such a configuration occurs, the four  $z$  roots of the characteristic equation  $H(z) - \epsilon_0 = 0$  with respect to an arbitrary point [blue point in Fig. 7(a)] on the OBC spectral portion are illustrated in Fig. 7(b), where  $z_2$  and  $z_3$  lie on the GBZ and have moduli greater than 1. Given that the winding number  $W_s = -1$ , this indicates the presence of a single zero inside the BZ contour. Consequently, one of the roots, say  $z_1$ , must be enclosed by the BZ. If we continuously deform  $\epsilon_0$  along an arbitrary path [e.g., the orange arrow in 7(a)] toward the PBC spectrum, the corresponding roots  $z_2$  and  $z_3$  will move away from the GBZ—one (e.g.,  $z_2$ ) evolves inward, and the other (e.g.,  $z_3$ ) evolves outward. This behavior is constrained by the requirement that the GBZ must enclose exactly two zeros of the characteristic equation in order to ensure a vanishing winding number of the OBC spectrum for any  $\epsilon_0$  that does not belong to the OBC spectrum [13]. Eventually,  $\epsilon_0$  and  $z_2$  will reach the PBC spectrum and the BZ, respectively, where the distribution of the four roots is given by  $|z_1| \leq |z_2| = 1 < |z_3| \leq |z_4|$ . We stress that  $z_2$ , rather than  $z_1$ , must arrive at the BZ when  $\epsilon_0$  reaches the PBC spectrum. This requirement arises because if  $z_1$  reaches the BZ while  $z_2$  remains outside, any infinitesimal deviation of  $\epsilon_0$  outside the PBC spectral loop cannot guarantee  $z_2$  entering the BZ—a necessary condition for achieving a vanishing winding number of the PBC spectrum. Since the leading term of Eq. (35) in such case is only one associated with  $z_4^L z_3^L$ , which cannot form a continuous band, the spectral and BZ configurations in Fig. 7 are suppressed. Following the same discussion, the PBC spectrum spectral and BZ configurations given in the main text exhibit the distribution of the four roots as  $|z_1| \leq |z_2| < |z_3| = 1 \leq |z_4|$ . The two leading terms of Eq. (35) are associated with  $z_4^L$  and  $z_4^L z_3^L$ , which allow for the formation of a continuous band. This PBC spectral portion, along with the associated BZ segment, is therefore physically permissible. Notably, since there are no constraints suppressing the contributions from  $z_1$ ,  $z_2$ , and  $z_4$ , the plane-wave component associated with  $z_3$  does not dominate the eigenstate. As a result, the eigenstates corresponding to the PBC spectral portion exhibit non-uniform spatial distributions.

In conclusion, under the CBCs with  $(\lambda_R, \lambda_L) = (0, 1)$ , we obtain the right-localized skin modes associated with the GBZ segment lying outside the unit circle (i.e., with modulus greater than 1), and the non-uniform eigenstates corresponding to the PBC spectral portion, which is associated with the BZ segment complementing the GBZ to form a closed GBZ' (BZ-GBZ composite). An analogous analysis for the CBCs with  $(\lambda_R, \lambda_L) = (1, 0)$  yields left-localized skin modes arising from the GBZ segment inside the unit circle (modulus less than 1), and non-uniform eigenstates corresponding to the PBC spectral portion associated with the remaining BZ segment.

### III. BOUNDARY-INDUCED COLLAPSE OF SPECTRAL LOOPS

In this section, we demonstrate the spectral collapse process from PBCs to CBCs in the paradigmatic model presented in the main text. In Fig. 8(a) [Fig. 8(b)], we decrease  $\lambda_R$  ( $\lambda_L$ ) from its PBC value while keeping  $\lambda_L = 1$  ( $\lambda_R = 1$ ) fixed. This implies a continuous collapse from the PBC spectral (purple) loops to the CBC (green) spectrum. Moreover, the parameters  $\lambda_R$  and  $\lambda_L$  control the collapse of the left and right PBC spectral loops, respectively, while keeping the opposite loops intact. Upon verification, the invariant portions of the PBC spectrum correspond to eigenstates that are nearly identical to those shown in the main text. In contrast, the spectral portions that collapse from the PBC loops to the OBC arcs are associated with eigenstates exhibiting a transition from plane-wave-like profiles to skin modes.

Remarkably, as long as  $\lambda_R$  or  $\lambda_L$  is nonzero, the two ends of the one-dimensional (1D) chain are effectively connected

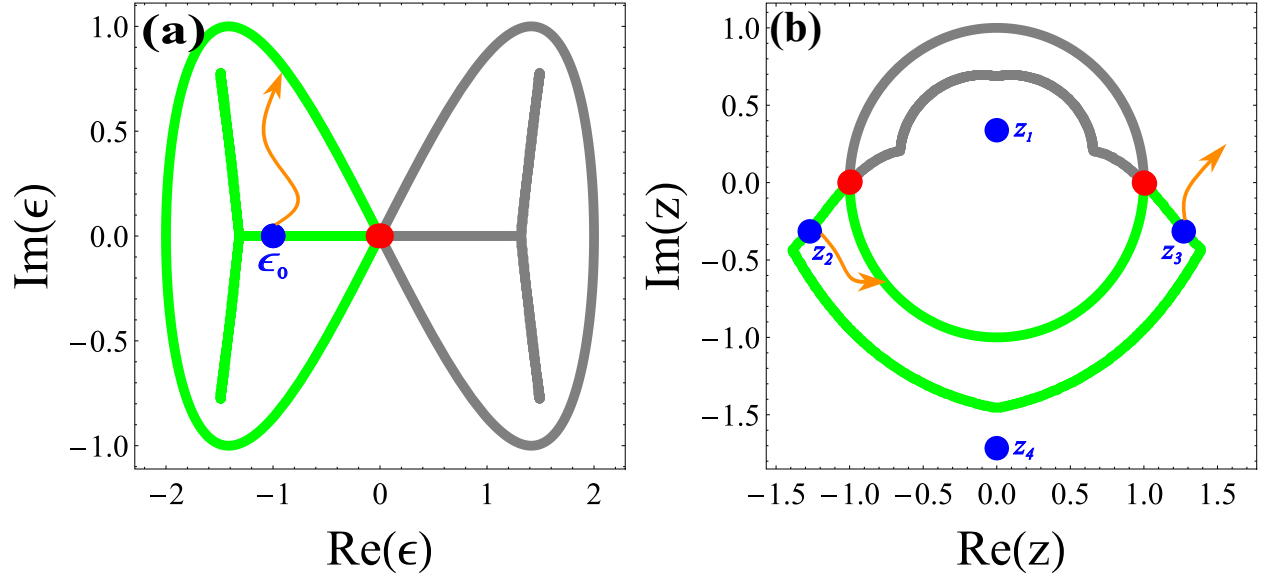


FIG. 7. Schematic illustration of spectrum suppression in green parts under CBCs with  $(\lambda_R, \lambda_L) = (0, 1)$ . (a) The blue point represents a selected energy on the OBC spectrum. (b) The blue points denote the corresponding four roots of the characteristic equation. Red points indicate the Bloch points on the spectrum and GBZ. The orange arrows trace the evolution of the energy and its associated roots of the characteristic equation, as considered in our analysis.

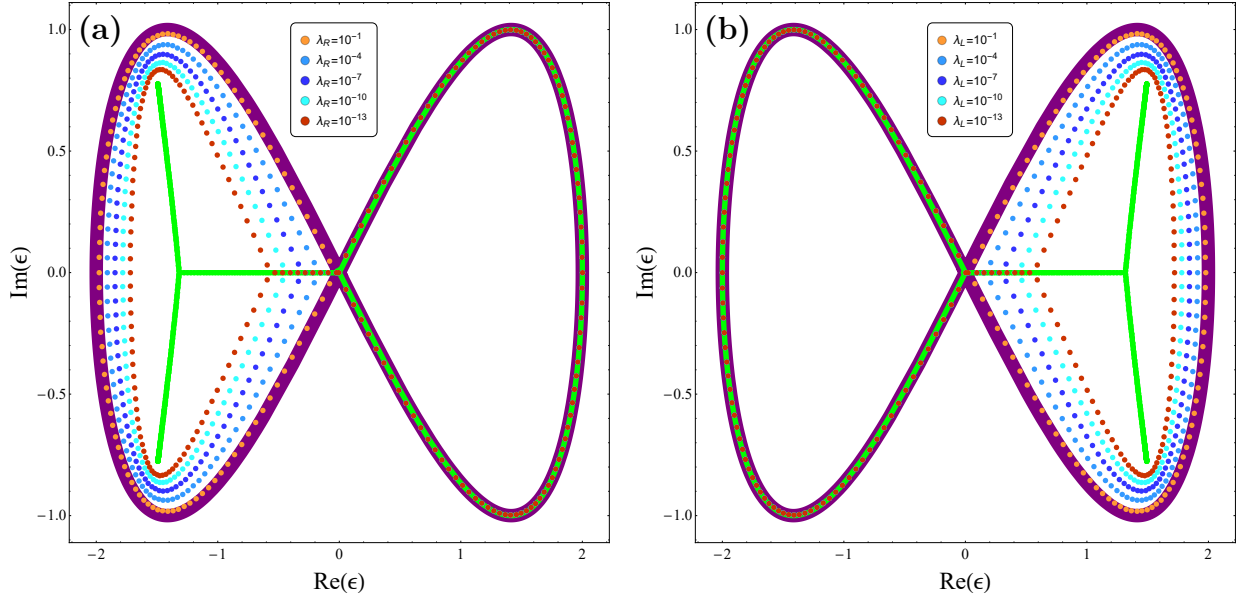


FIG. 8. The spectral collapse process from PBC to CBC spectra controlled by  $\lambda_R$  and  $\lambda_L$  in panels (a) and (b), respectively. The spectra with  $\lambda_{R,L} \neq 0, 1$  are numerical results obtained through a chain of 200 sites.

(quasi-PBC), giving rise to (thermodynamics-limit) loop structures in the corresponding part of the energy spectrum that indicate unidirectional, nonzero velocity. The magnitude of  $\lambda_R$  or  $\lambda_L$  controls the strength of this connection, thereby influencing both the size of the loop and the associated velocity. Only when  $\lambda_R$  or  $\lambda_L$  vanishes does the corresponding part of the spectrum collapse to its OBC counterpart [green arcs in Figs. 8(a) and 8(b)]. Thus, the spectral winding numbers (whether nonzero or zero) implicitly encode the topological configurations of certain spectral regions—manifested as loops or arcs—corresponding to the connection or disconnection of the chain's ends and the presence or absence of net velocities. The specific parameter values controlling the chain's ends modulate the non-topological details of the spectra.

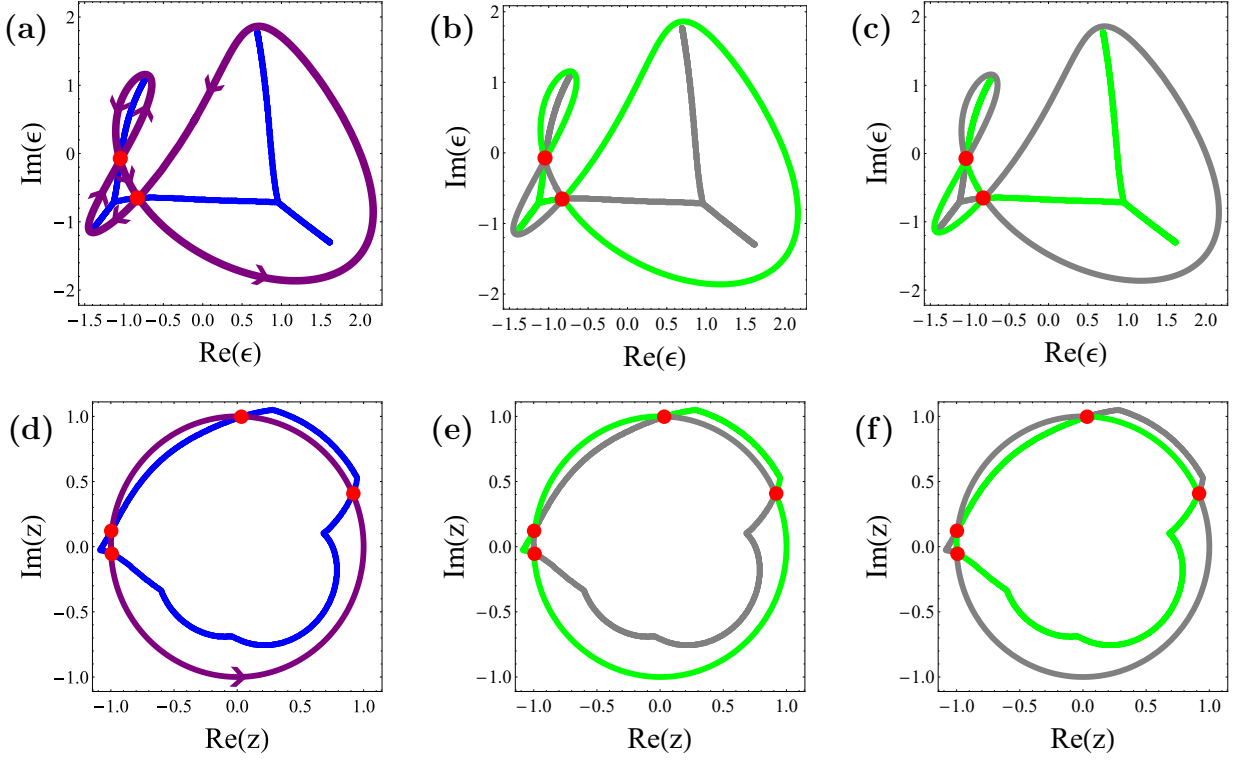


FIG. 9. The winding-control process of a model with three PBC loops as described by Eq. (36). (a) Spectra under PBCs (purple) and OBCs (blue). (b), (c) Spectra under CBCs with  $(\lambda_R, \lambda_L) = (0, 1)$  and  $(1, 0)$ , respectively (green curves). (d) The BZ (purple) and GBZ (blue). (e), (f) The GBZs' (green loops) exhibit a four-segment adjacency structure between each pair of neighboring Bloch points, corresponding to the CBC cases shown in (b) and (c), respectively. The regions with winding number  $W_s = +1, -1$ , and  $+1$  are enclosed by their respective PBC spectral loops. Red points indicate the Bloch points, while gray parts highlight the portions of PBC and OBC spectra (or BZ and GBZ) that are discarded under CBCs.

#### IV. WINDING CONTROL ACROSS MULTIPLE PBC SPECTRAL LOOPS

To demonstrate the broad applicability of our winding-control mechanism, we present a more intricate model, described by the Hamiltonian

$$\hat{H}_t = \sum_x \left[ ic_x^\dagger c_{x+1} - \frac{1}{2} ic_{x+1}^\dagger c_x - c_x^\dagger c_{x+2} + \frac{1}{2} c_{x+2}^\dagger c_x + \frac{1}{5} (c_x^\dagger c_{x+3} + c_{x+3}^\dagger c_x) \right], \quad (36)$$

with  $\lambda_{R,L} \in [0, 1]$  tuning the right/left boundary couplings analogous to the parametrization in the main text. The PBC spectrum  $H_t(z) = iz - iz^{-1}/2 - z^2 + z^{-2}/2 + (z^3 + z^{-3})/5$  with  $z \in \text{BZ}$  traces a three-loop self-intersecting closed curve [purple loops in Fig. 9(a)]. The OBC spectrum  $H_t(z)$  with  $z \in \text{GBZ}$  [blue arc in Fig. 9(a)] intersects the PBC curve at two Bloch points [red points in Fig. 9(a)], which corresponds to four intersection points [red points in Fig. 9(d)] between the BZ [purple loop in Fig. 9(d)] and the GBZ [blue loop in Fig. 9(d)]. The regions enclosed by the three spectral loops—separated by two Bloch points—exhibit winding numbers  $W_s = +1, -1$ , and  $+1$  in sequence, with each pair of adjacent loops carrying opposite winding numbers, as illustrated in Fig. 9(a).

As shown in Figs. 9(b) and 9(c), switching  $\lambda_R$  ( $\lambda_L$ ) from 1 to 0 causes the collapse of the PBC spectral loops with winding number  $W_s = -1$  ( $+1$ ) onto their corresponding OBC counterparts. Remarkably, the associated GBZ' exhibits a four-segment adjacency structure between each pair of neighboring Bloch points [Figs. 9(e) and 9(f)]. Moreover, by continuously tuning  $\lambda_R$  or  $\lambda_L$ , one can achieve a smooth interpolation between the corresponding PBC and OBC counterparts within the same winding-number regions, analogous to the behavior shown in Sec. III. Such winding-control process can also be implemented across the entire OBC spectrum via the similarity transformation, in the same manner as demonstrated in the main text.

## V. WINDING-CONTROL SPECTRUM OF TWO JOINT CHAINS

In this section, we demonstrate the extension of our winding-control spectrum mechanism via a joint-chain construction. As a first example, we consider the joint of two Hatano-Nelson (HN) chains embedded in the diagonal blocks of a real-space Hamiltonian, connected through arbitrary but nonzero off-diagonal couplings. Each chain is characterized by a different non-Hermiticity parameter  $\gamma$ , governed by the Hamiltonian

$$\hat{H}_{HN} = \sum_x \left[ (1 + \gamma)c_x^\dagger c_{x+1} + (1 - \gamma)c_{x+1}^\dagger c_x \right], \quad (37)$$

The spectra of the two chains are separated by a Fermi surface at chemical potential  $\mu$  [orange and purple loops in Fig. 10(a)]. The harmonious winding direction [gray region in Fig. 10(a)] enables a connection between the two chains, thereby preserving a loop-like spectral configuration across the corresponding real-valued Fermi surface—represented by the central green loop in Fig. 10(b). In contrast, the other regions exhibit inconsistent winding directions, leading to a spectral collapse into OBC-like arcs [Fig. 10(b)].

In the second example, we consider a joint system composed of a HN model with a specific  $\gamma$  and a non-Hermitian Su-Schrieffer-Heeger (NH-SSH) model defined on a bipartite lattice with sublattices  $A$  and  $B$ . The NH-SSH Hamiltonian is given by

$$\hat{H}_{nssh} = \sum_x \left[ \left( t_1 + \frac{2}{3} \right) c_{x,A}^\dagger c_{x,B} + \left( t_1 - \frac{2}{3} \right) c_{x,B}^\dagger c_{x,A} + c_{x,B}^\dagger c_{x+1,A} + c_{x+1,A}^\dagger c_{x,B} \right]. \quad (38)$$

Similarly, the two chains are embedded in the diagonal blocks of a real-space Hamiltonian and are connected via arbitrary but finite off-diagonal couplings. The regions with winding harmony preserve the loop-like spectral features of the NH-SSH model under PBCs, while regions with winding mismatch lead to a spectral collapse into OBC-like arcs [Figs. 10(c) and 10(d)].

The two examples above highlight the wider extension and applicability of our winding-control mechanism. Additionally, the rigorous analytical treatment and experimental realization of such joint-chain constructions represent key challenges and opportunities for future studies.

---

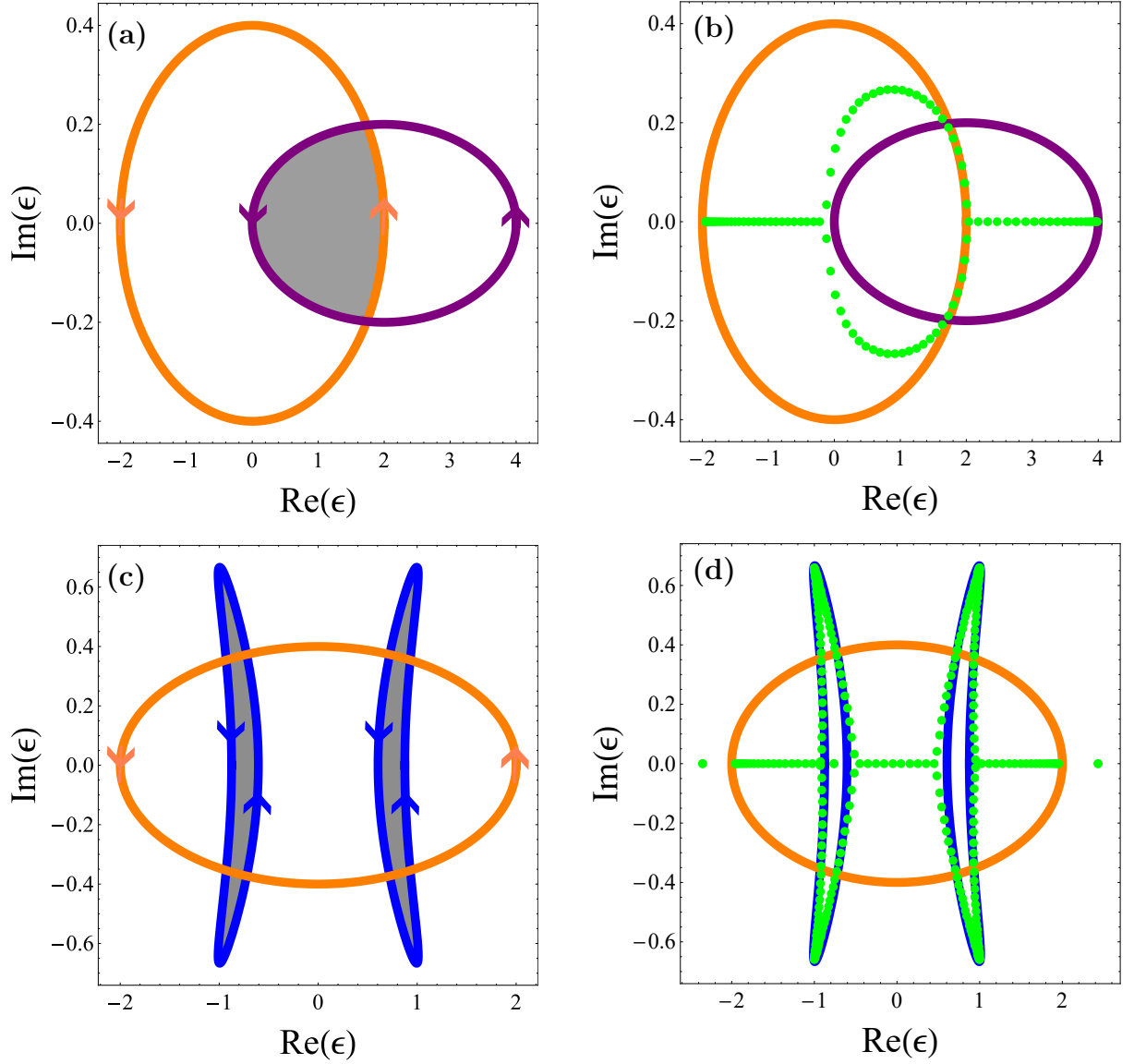


FIG. 10. (a) and (b): the two joint HN chains with distinct chemical potentials  $\mu = 0, 2$  and parameters  $\gamma = 0.2, 0.1$ . In panel (a), the PBC spectra are depicted as orange and purple loops, with the winding directions indicated. In panel (b), the exact diagonalization spectrum of the joint chain with 100 sites is shown as a green points. (a) and (b): the joint HN ( $\gamma = 0.2$ ) and NH-SSH ( $t_1 = 0.1$ ) chain. In panel (c), the PBC spectra shown in orange and blue loops, with the winding directions indicated. In panel (d), the exact diagonalization spectrum of the joint chain with 180 sites is shown as a green points. The winding-harmony regions are highlighted in gray.